Breast Cancer Reaction-Diffusion from Spectral-Spatial Analysis in Immunohistochemistry

Stefano Pasetto[1]*, Mohammad U. Zahid[1], Roberto Diaz[2], Michael Montejo[2], Marilin Rosa[3], Robert Gatenby[1,4], Heiko Enderling[1,2,5]

Departments of [1]Integrated Mathematical Oncology, [2]Radiation Oncology, [3]Pathology, [4]Radiology, [5]Genitourinary Oncology, H. Lee Moffitt Cancer Center and Research Institute;12902 Magnolia Drive, Tampa, FL 33612, United States of America
E-mail: stefano.pasetto@moffitt.org

Received xxxxxx
Accepted for publication xxxxxx
Published xxxxxx

Abstract

Cancer is a prevalent disease, and while many significant advances have been made, the ability to accurately predict how an individual tumor will grow – and ultimately respond to therapy – remains limited. We use spatial-spectral analysis of 20 patients accrued to a phase II study of preoperative SABR with 9.5 x 3 Gy for early-stage breast cancer whose tissues were stained with multiplex immunofluorescence. We employ the reaction-diffusion framework to compare the data-deduced two-point correlation function and the corresponding spatial power spectral distribution with the theoretically predicted ones. A single histopathological slice suffices to characterize the reaction-diffusion equation dynamics through its power spectral density giving us an interpretative key in terms of infiltration and diffusion of cancer on a per-patient basis. This novel approach tackles model-parameter-inference problems for tumor-infiltration forecasting and classification and immediately informs clinical treatments.

1. Introduction

Cancer is a polymorphic system that evolves over many scales, from intracellular through signaling pathways, macromolecular trafficking, intercellular through cell-cell adhesion and communication, and tissue level through cell-extracellular matrix interaction mechanical forces (Hatzikirou *et al.*, 2012). The complex interaction and co-evolution of the tumor with the host immune system recently received significant attention from cancer therapies that boost the immune system's antitumor response. Therefore, it is imperative to characterize tumor topology and heterogeneity and its overall growth and invasion potential in the complex tissue environment.

Great attention has been given to a mathematical formalization of growth and diffusion processes for cancer (Gatenby and Gawlinski 1996). The most significant mathematical advancement in using continuous diffusion models to study cancer dynamics comes from brain cancer modeling (Swanson *et al.*, 2000, 2001, 2002, 2003). General studies of tissue invasion (hypotaxis) analyze wave solutions and the tracking of heat-shock proteins (Szymanska *et al.*, 2009), or hypoxic cell waves and the pseudo palisades (hypercellular regions) in glioblastoma (GBM) (Martinez-Gonzalez *et al.*, 2012) in connection with imaging (Wang *et al.*, 2009). Similarly, the morphing of the extracellular matrix architecture by breast cancer cell diffusion and infiltration has been demonstrated (Pally *et al.*, 2019). Diffusion equations have mainly been used in compartment model approaches, e.g., for evolution from low to high-grade glioma (Bogdańska *et al.*, 2017) and its response to radiotherapy fractionation (Henares-Molina *et al.*, 2017). More recently, reaction-diffusion equations have been deployed on the cellular level to simulate spatial cell size distributions and their influence on uptake rates (Gerlee and Nelander 2012, Klank *et al.*, 2018, Khetan *et al.*, 2019).

In most of these works, diffusion models are assumed as an instrument to interpret a clinical condition (e.g., the anamnesis of a patient, a longitudinal past collection of data,

and similar) and forecast tumor dynamics with and without therapeutic interventions. A remarkable example is a study of DTI-MRI derived brain biomechanics that can predict the location of secondary cancer foci distant to the primary tumor (Angeli *et al.*, 2018).

No less important is the role of the diffusion process models in the approach to the clinically significant problems of patient-specific imaging-derived predictive models in response to neoadjuvant therapy of breast cancer. Several authors studied this problem (Weis *et al.*, 2013, 2015, 2017, Roque *et al.*, 2018, Jarrett *et al.*, 2018, Mang *et al.*, 2020), focusing on the coupling diffusion model to extracellular matrix stiffness, in connection with radiotherapy (Roniotis *et al.*, 2012, Holdsworth *et al.*, 2012, Borasi *et al.*, 2016) or synergy of radiation therapy and chemotherapy (Kibis and Buyuktahtakin 2018), surgical resection (Hathout *et al.*, 2016), necrosis density thresholds (Patel and Hathout 2017), radiation-induced necrosis (Narasimhan *et al.*, 2019), in vitro treatment of triple-negative breast cancer cell lines (Bowers *et al.*, 2020), in connection with in vitro growth (Ayensa-Jiménez *et al.*, 2020) or synthetic models of solid tumors (Sego *et al.*, 2020).

Parallel to this exploding interest in imaging, and thanks to the new or enhanced information from these new techniques, is the effort to develop new and more effective mathematical and statistical methodologies that can extract the correct information from this wealth of data. We present a technique that contributes to interpreting these data in this work. Nevertheless, the technique is generalizable and applicable to any imaging set and limited neither to 2D images nor to cancer diseases. In what follows, we will focus on imaging analysis of stained histopathological slides sampled from breast cancer patients. We analyze the spatial cell distribution of patient histopathology-stained slides (Fig. 1A) with the 2-point correlation function. This statistical tool introduced in the next section will show how cancer cell density varies as a function of the distance $\boldsymbol{r}$ from any cell (Riley *et al.*, 2006). Three Regions of Interest (ROI) are selected, including tumor ($\boldsymbol{\mathcal{T}}$), stroma distant to the tumor ($\boldsymbol{\mathcal{S}}$), tumor and stroma interface ($\boldsymbol{\mathcal{T}} - \boldsymbol{\mathcal{S}}$, Fig. 1B).

2. Methods

2.1 Patient data

A total of $\boldsymbol{N_{\mathrm{pat}} = 20}$ patients have been accrued to a Phase II Study of preoperative SABR with three times 9.5 Gy for early-stage breast cancer (NCT03137693). A 5 µm thick unstained tumor slide from formalin-fixed paraffin-embedded tumor block was acquired from biopsy and post-SABR and analyzed by the Moffitt Cancer Center tissue core and digital imaging laboratory. Tissues were stained with multiplex immunofluorescence to evaluate the infiltration of antigen-presenting cells, T-cells, NK cells, B-cells, and tumor cells using different combinations of CD3 and CD4 CD8, Foxp3, PD-1, CD68, PanCytoKeratin (PCK). For six patients, we have both pre-and post-treatment data. We focus on this subset of patients in the main text, leaving to Supplement 1 the investigation of patients with either pre-or post-treatment alone.

2.2 2-point correlation function

We implement the 2-point correlation function (2pCF) as a spatial statistic estimator for our histopathology tissue slices (Ridgway et al., 2006; Mosaliganti et al., 2009; Cooper et al., 2010, 2011; Binder & Simpson, 2015). The spatial *n*-point autocorrelation function $\boldsymbol{c_{np}}$ is defined as the probability of finding *n* cells at coordinates $\mathbf{x_1}$, $\mathbf{x_2}$, …, $\mathbf{x_n}$ in a suitably defined reference frame $\boldsymbol{S}(\boldsymbol{O}, \mathbf{x})$ centered in $\boldsymbol{O}$ with $\mathbf{x_i} = \{\boldsymbol{x_1}, \boldsymbol{x_2}, \boldsymbol{x_3}\}_{\boldsymbol{i}}$ as spatial coordinates for the $\boldsymbol{i} = \mathbf{1}, \mathbf{2}, \mathbf{3}, \ldots, \boldsymbol{n}$. If we refer to the cell type $\boldsymbol{j}$, $\boldsymbol{j} \in \boldsymbol{T}$ with $\boldsymbol{T}$ set of possible cell types $\boldsymbol{T} = \{\boldsymbol{\mathcal{T}}, \boldsymbol{\mathcal{S}}, \boldsymbol{CD3^+}, \boldsymbol{CD4^+}, \boldsymbol{CD8^+}, \boldsymbol{FOXP3}, \ldots\}$, where $\boldsymbol{\mathcal{T}}$ refers to tumor cell population, $\boldsymbol{\mathcal{S}}$-stroma cell population, and so forth. Then for the generic set type $\boldsymbol{j}$ in our histopathology-stained slide, we can formalize $\boldsymbol{c_{np}^{(j)}}$ as $\boldsymbol{c_{np}^{(j)}} = \langle \boldsymbol{\delta}(\mathbf{x_1})\boldsymbol{\delta}(\mathbf{x_2}), \ldots, \boldsymbol{\delta}(\mathbf{x_n})\rangle^{(j)}$([1]).

We focus on the 2pCF of the cancer population. We drop index $\boldsymbol{j}$ and refer to the 2pCF as the auto-correlation function. Furthermore, because of the connection we are going to develop in the next section with the continuous RD equation, we are going to implement for the 2pCF the following definition ([2]):

$$\boldsymbol{c_{2p}}(\mathbf{r}, \boldsymbol{\tau}) = \frac{\langle (\boldsymbol{\rho}(\mathbf{x}+\mathbf{r}, \boldsymbol{t}+\boldsymbol{\tau}) - \langle \boldsymbol{\rho} \rangle)(\boldsymbol{\rho}(\mathbf{x}, \boldsymbol{t}) - \langle \boldsymbol{\rho} \rangle) \rangle}{\langle \boldsymbol{\rho} \rangle^2}, \qquad (1)$$

with $\langle \boldsymbol{\rho} \rangle = \boldsymbol{n}$ the average number of cells for volume unit, $\boldsymbol{r} = \|\mathbf{r}\| \equiv \|\mathbf{x_1} - \mathbf{x_2}\|$, and $\boldsymbol{\tau}$ is a time interval. Because we work with a single breast cancer histopathology slice, we

1 Note how the significant differences between npCf and cooccurrence (Haralick et al., 1973) are, aside from normalization factors, the pixeled/grid-free definition of the npCf and the possibility to capture both geometry and statistical nature of the images analyzed without grey-levels definition.

2 We note that the definition of the correlation function (or of the covariance function, or its relation with the Ripley's K function) is not universal across the different disciplines and textbooks: the subtraction of the average density or any uncorrelated average product of 2 random variables is a matter of convention that, therefore we fix here with this definition.

cannot sample the same tissue section twice, and we cannot consider the time dependence of the autocorrelation. Therefore we simplify Eq.(1) to:

$$\langle \boldsymbol{\rho}(\mathbf{x}+\mathbf{r})\boldsymbol{\rho}(\mathbf{x})\rangle = \boldsymbol{n}^2\left(\mathbf{1}+\boldsymbol{c}_{2p}(\boldsymbol{r})\right). \quad (2)$$

The interpretation of this type of correlation function is simple: if the probability of finding a cell in the volume $\boldsymbol{dV}$ is $\boldsymbol{dP} = \boldsymbol{ndV}$ with $\boldsymbol{n}$ the average number of cells in the finite volume spanned by the histopathology slide, then $\langle \boldsymbol{N}\rangle = \boldsymbol{nV}$ and the joined probability of finding two cells say cell 1 and cell 2, at a given distance $\boldsymbol{r}$, is

$$\boldsymbol{dP} = \boldsymbol{n}^2\boldsymbol{dV}_1\boldsymbol{dV}_2\left(\mathbf{1}+\boldsymbol{c}_{2p}(\boldsymbol{r})\right), \quad (3)$$

which gives us also a concept interpretative key: If the cell distribution is a 3D random Poisson point process, the probability of finding cells in $\boldsymbol{dV}_1$ and $\boldsymbol{dV}_2$ are independent, in this case $\boldsymbol{c}_{2p} = \mathbf{0}$, if the cell positions are correlated $\boldsymbol{c}_{2p} > \mathbf{0}$, and if the positions are anticorrelated $\boldsymbol{c}_{2p} \in [-\mathbf{1}, \mathbf{0}[$.

Note that to properly account for the 3D overlapping of cells in the spatial analysis of the 2pCF, we augmented Eq. (2) with several kernels, boundary conditions, and bandwidth, always finding convergence (but not coincidence) of results. We refer the reader to the technical treatment offered in Supplement 1.

2.3 Power spectrum of the fluctuations

For a continuous function, the Fourier transform of the autocorrelation function is the power spectrum. We only review the analogous for a 3D random point process we use in the following, focusing on and developing only the equations of interest (Alessio 2016). The Fourier transform for the distribution of cells with density $\boldsymbol{\rho}(\mathbf{x},\boldsymbol{t}) = (\langle\boldsymbol{\rho}\rangle\boldsymbol{V})^{-1}\sum_i \boldsymbol{\delta}\left(\mathbf{x}-\mathbf{x}_i(\boldsymbol{t})\right)$ is

$$\boldsymbol{\delta}_{\mathbf{k}} = (\boldsymbol{nV})^{-1}\sum_i \ \boldsymbol{e}^{\boldsymbol{\iota}\mathbf{k}\cdot\mathbf{x}_i}, \quad (4)$$

with wavenumber $\boldsymbol{k} = \|\mathbf{k}\|$ with $\|*\| = \|*\|_2$ Euclidean norm., $\mathbf{k} = \{\boldsymbol{k}_x, \boldsymbol{k}_y, \boldsymbol{k}_z\}$, where the barycenter of the ith cell is located at $\mathbf{x}_i$ and $\boldsymbol{e}^{\boldsymbol{\iota}\mathbf{k}\cdot\mathbf{x}}$ is periodic in $\boldsymbol{V}$ ($\boldsymbol{\iota}$ is the complex imaginary units, "·" the inner product). We slice the volume $\boldsymbol{V}$ (we refer to the slice and its volume with the same symbol $\boldsymbol{V}$ without loss of generality) into infinitesimal cells with unitary function $\mathbf{1}_{dV}$ ($\mathbf{1}_{dV} = \mathbf{1}$ if the cell is in the volume $\boldsymbol{V}$, or $\mathbf{1}_{dV} = \mathbf{0}$ if it is not). Therefore Eq. (4) is equivalent to

$$\boldsymbol{\delta}_{\mathbf{k}} = (\boldsymbol{n}\mathbf{V})^{-1}\sum_i \ \mathbf{1}_{d\mathbf{V}}\boldsymbol{e}^{\boldsymbol{\iota}\mathbf{k}\cdot\mathbf{x}_i}. \quad (5)$$

Hence, the averaged two-cells contribution to the spectrum of wavelengths, say cell $\mathbf{1}$ in $\boldsymbol{dV}_1$ and cell 2 in $\boldsymbol{dV}_2$, reads:

$$(\boldsymbol{nV})^2\langle\boldsymbol{\delta}_{\mathbf{k}}\boldsymbol{\delta}_{-\mathbf{k}'}\rangle = \sum\langle\mathbf{1}_1^2\rangle\boldsymbol{e}^{\boldsymbol{\iota}(\mathbf{k}-\mathbf{k}')\cdot\mathbf{x}_1} + \sum\langle\mathbf{1}_1\mathbf{1}_2\rangle\boldsymbol{e}^{\boldsymbol{\iota}(\mathbf{k}\cdot\mathbf{x}_1-\mathbf{k}'\cdot\mathbf{x}_2)}$$

$$= \boldsymbol{n}\int_{\mathbb{R}^3}\boldsymbol{dV}\boldsymbol{e}^{\boldsymbol{\iota}(\mathbf{k}-\mathbf{k}')\cdot\mathbf{x}_1}$$

$$+\boldsymbol{n}^2\int_{\mathbb{R}^3}\boldsymbol{dV}_1\boldsymbol{dV}_2\left(\mathbf{1}+\boldsymbol{c}_{2p}\right)\boldsymbol{e}^{\boldsymbol{\iota}(\mathbf{k}\cdot\mathbf{x}_{12}+(\mathbf{k}-\mathbf{k}')\cdot\mathbf{x}_2)}, \quad (6)$$

because $\langle\mathbf{1}_1\mathbf{1}_2\rangle = \boldsymbol{n}^2\boldsymbol{dV}_1\boldsymbol{dV}_2\left(\mathbf{1}+\boldsymbol{c}_{2p}\right)$ as results of considering Eq. (3) (with $\mathbf{x}_{12}$ Euclidean distance between cell 1 and 2). Because Fourier components belonging to different $\mathbf{k}$ are statistically independent, the integrals in the previous vanishes if $\mathbf{k} \neq \mathbf{k}'$, while for $\mathbf{k} = \mathbf{k}'$ yields, as a well known results, the spectrum (the power spectral density, PSD) of the cell distribution:

$$\mathbf{P}(\boldsymbol{k}) \equiv \langle|\boldsymbol{\delta}_{\mathbf{k}}|^2\rangle = \int_{\mathbb{R}^3}\frac{\boldsymbol{d}^3\mathbf{x}}{\mathbf{V}}\boldsymbol{c}_{2p}(\boldsymbol{r})\boldsymbol{e}^{\boldsymbol{\iota}\mathbf{k}\cdot\mathbf{x}} + \frac{\mathbf{1}}{\boldsymbol{n}\mathbf{V}}, \quad (7)$$

for $\boldsymbol{k} \neq \mathbf{0}$, and $\langle|\boldsymbol{\delta}_{\mathbf{0}}|^2\rangle = \int_{\mathbb{R}^3}\frac{\boldsymbol{d}^3\mathbf{r}}{\mathbf{V}}\boldsymbol{c}_{2p} + \frac{\mathbf{1}}{\boldsymbol{n}\mathbf{V}}$, otherwise. The power spectrum measures the mean number of neighbors in excess of a random Poisson distribution within a distance of $\sim\boldsymbol{k}^{-\mathbf{1}}$ of a randomly chosen cell. This classical result (Peebles 1973) is often coupled with filter-design windows functions commonly implemented in the power spectrum determination to optimize its analytical treatment (Dirichlet, Hamming, Blackman, etc.) that we also tested (see Supplement 1) with consistent results. In this paper, we will stick to the derivation presented above. Nuttall-softening length (Nuttall 1981) will be preferred if necessary.

2.4 2-point correlation function from the reaction-diffusion equation

Diffusion of a cluster of cells with density $\boldsymbol{\rho} = \boldsymbol{\rho}(\mathbf{r},\boldsymbol{t})$ at position $\mathbf{r}$ and at time $\boldsymbol{t}$ is described by the combination of the continuity equation without source and sink terms as $\boldsymbol{\partial}_t\boldsymbol{\rho} + \boldsymbol{\nabla}.\boldsymbol{\varphi} = \mathbf{0}$ (with $\boldsymbol{\partial}$ being the partial derivative and $\boldsymbol{\nabla}$ the gradient operator) and Fick's first law of proportionality between flux $\boldsymbol{\varphi}$ and density gradient $\boldsymbol{\nabla\rho}$, $\boldsymbol{\varphi} = -\boldsymbol{\mathcal{D}}.\boldsymbol{\nabla\rho}$, to get (for a generic anisotropic flow) $\boldsymbol{\partial}_t\boldsymbol{\rho} = -\boldsymbol{\nabla}.(\boldsymbol{\mathcal{D}\nabla\rho})$ where $\boldsymbol{\mathcal{D}}$ is a diffusion coefficient matrix. In a 3D system of reference (SoR) $\boldsymbol{S}(\boldsymbol{O}, \mathbf{r} = \{\boldsymbol{x},\boldsymbol{y},\boldsymbol{z}\})$, with $\boldsymbol{r}^2 = \boldsymbol{x}^2+\boldsymbol{y}^2+\boldsymbol{z}^2$ being the squared radial direction from an arbitrary origin $\boldsymbol{O}$, we can write the diffusion equation for the locally homogeneous and isotropic case as $\boldsymbol{\partial}_t\boldsymbol{\rho} = \boldsymbol{\mathcal{D}\nabla}^2\boldsymbol{\rho}$, where $\boldsymbol{\nabla}^2$ is the D'Albertian

operator. Green functions offer a natural solution for cell-like source points, even in the presence of an explicit exponential growth factor $\boldsymbol{\gamma}$, i.e., $\boldsymbol{\partial_t \rho = \mathcal{D}\nabla^2 \rho + \gamma \rho}$ of interest here, in the form:

$$\boldsymbol{\rho(\mathbf{r}, t) = \frac{\rho_0}{(4\pi\mathcal{D}t)^{\frac{3}{2}}} \mathbf{e}^{-\frac{\|\mathbf{r}\|^2}{4\mathcal{D}t} + \gamma t}}. \quad (8)$$

Note how this approach follows exponential tumor growth without carrying capacity constraints, and we will comment on this limitation later. For now, we focus on tumor RD statistics as an average over the tumor ROI, $\boldsymbol{\mathcal{T}}$. We assume that the cells are spread over a small volume $\boldsymbol{d^3\mathbf{r}}$ so that, as long as this volume is asymptotically smaller than the cell migration movement per unit time, i.e., to the first order in time, it holds $\boldsymbol{d\mathbf{r} \prec O(\sqrt{\mathcal{D}dt})}$, we can generalize the previous equation as $\boldsymbol{\rho(\mathbf{r}, t) = \rho_0 d^3\mathbf{r}(4\pi\mathcal{D}t)^{-\frac{3}{2}} e^{-\frac{\|\mathbf{r}\|^2}{4\mathcal{D}t} + \gamma t}}$. In the case of $\boldsymbol{n}$ different cells $\boldsymbol{\rho(\mathbf{r}, t) = (4\pi\mathcal{D}t)^{-\frac{3}{2}} \rho_{0i} \mathbf{e}^{-\frac{\|\mathbf{r}_i\|^2}{4\mathcal{D}t} + \gamma t} d^3\mathbf{r}}$ (where Einstein's muted index convention is assumed) or, in the passage to the continuous limit, we get the classical heat-equation result that we are going to exploit here for our RD problem:

$$\boldsymbol{\rho = \int_{\mathbb{R}^3} d^3\mathbf{r}' \rho_0(\mathbf{r}')(\mathcal{D}t)^{-\frac{3}{2}} e^{-\frac{\|\mathbf{r}-\mathbf{r}'\|^2}{4\mathcal{D}t} + \gamma t} = \rho_0 * f_{RDPS}}. \quad (9)$$

The last term in the equation is the one of interest here. The cell concentration at the generic time $\boldsymbol{t}$ is the convolution, denoted here by "*", of the initial concentration with a Gaussian, that by borrowing the terminology from Astronomy, we call RD point-spread-function $\boldsymbol{f_{RDPS}}$. Here cell concentration at $+\infty$ is assumed to be null. Furthermore, by assuming constant temperature and pressure in the tissue sample, we justify $\boldsymbol{\mathcal{D} = \mathbf{cnst}}$. and elaborate on the $\boldsymbol{f_{RDPS}}$ as the function that carries the temporal dependence.

To proceed further, we now adopt a "fair representation" hypothesis: we assume that histopathology slides, surgically acquired from a local resection area, are reasonably representative of the clustering properties of the total tumor population of the patient. We comment in the Discussion section more on the implication of this assumption that allows us to proceed with a mean-field solution for the RD equation over the histopathology slice volume. By performing this Gibbs-average, we assume that the volume over which the average is performed is large enough to contain a sufficient number of cells to perform statistical analyses but small enough to neglect large-scale gradients (i.e., $\boldsymbol{\mathcal{D} = \mathbf{cnst}}$. holds reasonably well). In this case, from Eq.(9) we obtain:

$$\boldsymbol{\langle \rho \rangle = \langle \rho_0 \rangle * \langle f_{RDPS} \rangle}, \quad (10)$$

where we define the average over the time of the RD spread function as:

$$\boldsymbol{f_{RD} \equiv \langle f_{RDPS} \rangle = \frac{1}{\Delta \mathbf{t}} \int_0^{\Delta \mathbf{t}} f_{RDPS}}, \quad (11)$$

with $\boldsymbol{\Delta \mathbf{t}}$ sufficiently small that will indeed account for the non-equilibrium dynamics of diffusion and proliferation required by the average in $\boldsymbol{\rho_0}$. The drawback of this approach is that the same patient presents constant different diffusion coefficients $\boldsymbol{\mathcal{D}}$, and growth rate $\boldsymbol{\gamma}$, in distinct resection areas instead of having continuous functions for $\boldsymbol{\mathcal{D} = \mathcal{D}(\mathbf{x}, t)}$ and growth rate $\boldsymbol{\gamma = \gamma(\mathbf{x}, t)}$ dependent on spatial position. Furthermore, stochastic correlation is different from $\boldsymbol{\mathcal{T}}$, and $\boldsymbol{\mathcal{S}}$ area (Fig. 1), and we expect the theory to break down at the $\boldsymbol{\mathcal{T} - \mathcal{S}}$ interface. Therefore, we are forced to solve the RD equation only locally in $\boldsymbol{\mathcal{T}}$. Finally, by considering the non-normalized autocorrelation of the average cell concentration $\boldsymbol{\langle \rho \rangle}$, we write

$$\boldsymbol{c_{2p} = \big((\rho_0 - \langle \rho_0 \rangle) * (\rho_0 - \langle \rho_0 \rangle)\big) * (f_{RD} * f_{RD}) = \sigma_\rho^2 (f_{RD} * f_{RD})}, \quad (12)$$

where the initial density is non-correlated, and the correlation function reduces to its variance $\boldsymbol{\sigma_\rho}$. The biological implication is that diffusing cells enhances cell proliferation – a visualization of loss of space and contact inhibition. Therefore, these reactions are stochastically correlated, and Eq. (12) assumes that cell diffusion is the only mechanism by which cells become spatially correlated. The autocorrelation of $\boldsymbol{f_{RD}}$ captures this spatial correlation thus not contradicting Eq.(10) as ergodicity does not imply mixing (Supplement 2).

2.5 Power spectrum from reaction-diffusion equation

The RD equation's analytical solution is unavailable for arbitrary reaction terms; therefore, it is easier to work with power spectral densities than with 2-point correlation functions to connect cancer diffusion with its spatial distribution. Performing Eq. (11) on Eq.(8), we obtain $\boldsymbol{f_{DR}}$ as

$$\boldsymbol{f_{RD} = \frac{e^{\iota\|\mathbf{x}\|\sqrt{\frac{\gamma}{\mathcal{D}}}}}{8\pi\mathcal{D}\|\mathbf{x}\|} \mathbf{erfc}\left(\frac{\|\mathbf{x}\|}{2\sqrt{\mathcal{D}\Delta t}} + \iota\sqrt{\gamma\Delta t}\right) + \frac{e^{-\iota\|\mathbf{x}\|\sqrt{\frac{\gamma}{\mathcal{D}}}}}{8\pi\mathcal{D}\|\mathbf{x}\|} \mathbf{erfc}\left(\frac{\|\mathbf{x}\|}{2\sqrt{\mathcal{D}\Delta t}} - \iota\sqrt{\gamma\Delta t}\right)} \quad (13)$$

where erfc(*) is the complementary error function. Finally, considering Eq. (12), Eq.(13) together with the definition of power spectral density, we obtain

$$\mathbf{P}(\boldsymbol{k}) \equiv \left|\int_{\mathbb{R}^3} \boldsymbol{d^3\mathbf{x} f_{RD} e^{\iota \mathbf{k}.\mathbf{x}}}\right|^2 = \boldsymbol{P_0^2} \left(\frac{\mathbf{e}^{(\gamma - \|\mathbf{k}\|^2\mathcal{D})\Delta t} - 1}{\Delta t(\gamma - \|\mathbf{k}\|^2\mathcal{D})}\right)^2, \quad (14)$$

where for easier comparison with Eq. (7) we normalized with $\boldsymbol{P_0}$ to the zero-wavelength by computing $\int_{\mathbb{R}^3} \mathbf{P}(\mathbf{k})\boldsymbol{d^3}\mathbf{k}$ to obtain our final result.

We finally perform an inference exercise of the model Eq. (7) to the PSD data with the same Bayesian/Frequentists techniques (Pasetto et al., 2021a). Any other inference approach is equally valid.

3. Results

3.1 Breast tumor detection by the 2-point correlation function

Using the previous section's methodology, we analyzed patient histopathology-stained spatial cell distribution (Fig. 1b). Qualitatively we can recap the trend evidenced across the dataset as follows.

The combined tumor and stroma cell distribution in a $\mathcal{T}$-ROI proposes a characteristic monomial distribution signature. Analysis of the spatial distribution of tumor cells alone follows a similar linear relationship in the bi-logarithmic plot. The correlation is mainly positive in both cases, meaning an architectural aggregation of the cells in the ROI exceeds the Poisson distribution (i.e., randomness). By contrast, cell clustering in stroma-dominated ROI, $\mathcal{S}$, presents a more rapid loss of positive correlation to favor an irregularly oscillatory 2pCF profile at about one order of magnitude smaller values -cross patients- than for $\mathcal{T}$-ROI. The 2pCF in $\mathcal{S}$-ROI approximates $c_{2p} \cong 0$, equivalent to a random cellular distribution, without any evident characteristic signature or regularity in the sample analyzed. Finally, the bi-logarithmic plot for intermediate $\mathcal{T} - \mathcal{S}$ ROI presents a monomial behavior at low-medium r, similar to what is evidenced for $\mathcal{T}$ ROI. Still, it shows an abrupt drop that characterizes it toward largely negative c_{2p} at asymptotically larger r (less clustered than a random distribution).

3.2 Radiation therapy induces changes in cancer cell distribution morphology

We analyze the spatial distribution of cancer cells in the different $\mathcal{T}$ ROI before (Fig. 2A) and after (Fig. 2B) SABR. We investigate $c_{2p} + 1$ to evaluate only positive values of the 2pCF. The Poisson-process threshold moves from 0 to 1, with $c_{2p} > 1$ representing spatial correlation or cell clustering, and $c_{2p} < 1$ representing anticorrelation for $\mathcal{T}$ cell distribution alone. Cancer cells in three different $\mathcal{T}$ ROI both pre-and post-treatment (referred to as A, B, and C in Fig 2 panel A, as well as D, E, and F in Fig. 2 panel B, respectively) strongly cluster in close neighborhoods ($r < 50$ μm) but lose positive correlation with a different characteristic slope as they approach Poisson randomness at more considerable distances ($r > 50$ μm; Fig. 2, second column). Furthermore, we consider the 2pCF Fourier transform introduced in the previous section, the power spectral density (PSD), to better capture the multiscale contribution to the cancer architectural organization (tracked by wavenumbers, k) across the resection area. The characteristic "white-noise" plateau at small wavenumbers is followed after a characteristic wavenumber value where the PSD shape bends downward (sometimes referred to as correlation-length) by the drop of the PSD at higher k (Fig. 2, third column).

3.3 The histopathology slides power spectrum analysis calibrates reaction-diffusion equation parameters

Patient tissues provide a single-time snapshot of the complex evolution of the cellular density in different spatial locations inside the resection area (Fig. 1). The exact location of each cancer cell and cancer cell conglomerates gives insights into the tumor proliferation and invasion dynamics. The reaction-diffusion (RD) equation represents a family of models relating the density of cancer cells in a given position at a given time as a function of the proliferation rate γ (per unit time) and a diffusion coefficient $\mathcal{D}$ (area per unit time). We used the derived analytical formulation of the PSD for the homogeneous-isotropic RD equation and solved the RD parameter inference problem by interpreting the observed PSD of the histopathology slides with the PSD derived from the RD equation. We note how the RD framework disentangles the contributions between proliferation and diffusion at different wavenumbers, optimizing the inference solution. In Fig. 3a, we show how different reaction rates mainly contribute, and hence disentangle, at low wavenumbers while the influence at high k is dominated by the diffusion coefficient. The PSD of the RD equation closely captures the PSD of the pre-and post-treatment tissues ($R^2 > 0.9$; Fig. 3b).

Furthermore, the RD framework disentangles the different contributions between proliferation and diffusion by systematic differences in pre and post-treatment PSD. A direct comparison of pre-and-post-SABR RD parameters demonstrates a reduction in the patient-specific diffusion parameter, $\mathcal{D}_{\text{pat}}$, for each patient normalized by the average patient-specific diffusion parameter, $\overline{\mathcal{D}_{\text{pat}}}$ (i.e., across all $\mathcal{T}$ ROI pre and post-SABR, Fig. 4A). However, the normalized patient-specific growth rate parameter showed a dichotomy of responses for the $\gamma_{\text{pat}} / \overline{\gamma_{\text{pat}}}$ trend: increasing for some and decreasing for other patients (Fig. 4B). In Fig. 4C, the ratio of the coefficients (not averaged) is shown to track the cumulative effect of disease diffusion and proliferation: SBRT may induce an increase in the ratio with expected tumor growth (patients #6, #9, #18), while a decreasing trend

suggests likely post-SBRT tumor regression (patient #4, #13, #20).

4. Discussion

Cancer is a complex adaptive dynamic system that evolves at multiple scales; therefore, a trans-levels technique that captures the characteristics of several scales (or equivalently over several wavenumbers) is of fundamental importance. Here we presented the first step in developing such an interpretative methodology to capture the dominant scale lengths that drive breast cancer architectures before and after stereotactic ablative radiotherapy. Herein, we explore the potential of the cancer-cell architecture-defragmentation analysis and interpret it as a growth and tissue invasion process through the RD equation. The two-point correlation function connects spatial architecture and tumor growth and diffusion. The power spectral density is obtained directly from patient tissue immunofluorescence histopathology slides to calibrate the parameters of the RD equation.

Such an approach requires a few theoretical and biological hypotheses, particularly the "fair representation" hypothesis that histopathology slides are reasonably representative of the clustering properties of the total tumor population. While the tumor's loco-regional properties may be well captured in an individual drop, the overall tumor is highly heterogeneous, and the cancer cell population's local characteristics might depend on the micro-environment. We assumed that the sampled ROI is representative of the overall patient disease. Furthermore, we adopted a "strong" version of the fair-representation hypothesis: we assumed that the analysis presented represents the characteristic of the disease type. The fair-representation hypothesis then permits us to generalize the consideration by comparing different patient biopsies and different patients, empowering our considerations. I.e., we assume that we are studying not one patient breast cancer but that we can extend our consideration to all breast cancers. Therefore, to achieve the goals of the present work, we took the validity of histopathology spatial characterization worked out with the 2pCF as fairly representing the nature of the breast cancer and considered average trends over the sample of patients available to us. This stretch will be tested when additional, more extended databases of breast cancer histopathology become available. While potentially conceived as a limitation; instead, this approach offers the possibility to control on a cell-by-cell basis the connection between spatial statistical tools, the two-point correlation function, and the corresponding power spectrum.

The second strong hypothesis is found in the choice of the interpretative framework: the RD equation. While the 2pCF and the corresponding PSD from the dataset are virtually free of assumption, the RD framework was not derived from the data but was chosen due to its simplicity. No reason a priori justifies the choice and form of the equation if not the practical analytical tractability, especially in Fourier space. While more physically involved approaches exist, such as Navier Stokes approaches, especially in the glioma literature (see introductive references), numerical investigation of integrative instruments and the power spectral density (which easily captures several orders of magnitude in wavelength) would involve multiscale physical parametrization that is not justified by the resolution and quantity of the available data. Thus, the chosen approach aligns with the clinical dataset and moves toward a predictive quantitative oncology framework. The clinical data set only provided matched pre-and-post-SBRT tissue samples for six patients with comparable outcomes for quantitative analysis. Therefore, the focus of this work is the development of breast cancer patient-specific reaction-diffusion dynamics from spectral analysis of immunohistochemistry slides. Future work will include analysis of such derived dynamics to predict complete pathological responses, relapse-free, and overall survival to help guide clinical decision-making (Pasetto et al., 2021b).

Finally, although beyond the scope of this study, it is conceivable that 2pCF analyses could help build a robust classifier to detect the presence of cancer architectures in selected biopsy ROI. Future work will include rigorous analysis of such digital pathology approaches.

5. Conclusion

Understanding tumor growth and invasion dynamics are paramount to personalizing patient care and improving outcomes. We developed a novel quantitative approach to infer such dynamics characteristics from a single biopsy taken at patient diagnosis. Inspired by looking at Fig. 4, we can easily envisage that for a patient described by a high proliferative index and a low diffusivity, we need to act with a targeted local aggressive therapy (e.g., radiation therapy). Vice versa, for a slowly proliferating cancer but highly diffusive and prone to metastasis, we want to proceed with systemic treatments (e.g., immunotherapy, chemotherapy). This result represents a fundamental step toward integrating quantitative methods into clinical decision-making to improve treatment responses and outcomes(Pasetto *et al.*, 2021b). In the future, we aim to extend the database size, and the type of cancer analyzed to transform the simple indications of Fig. 4 into a robust instrument able to predict the cancer evolution with achieved accuracy statistically.

Acknowledgments

The authors would like to thank Isha Harshe for her help with Fig. 1. Funding: This work was supported by NIH/NCI grant U01CA244100; the Florida Breast Cancer Foundation; the JAYNE KOSKINAS TED GIOVANIS FOUNDATION FOR HEALTH AND POLICY, a private foundation committed to critical funding of cancer research. The opinions, findings, conclusions, or recommendations expressed in this material are those of the author(s) and not necessarily those of the JAYNE KOSKINAS TED GIOVANIS FOUNDATION FOR HEALTH AND POLICY, or their respective directors, officers, or staffs.

Ethical statement

This study met the approval of the institutional review board, protocol MCC 18383: "Treatment Outcomes of Breast Cancer Patients Treated with All or One of the Multimodality Therapies at H. Lee Moffitt Cancer Center & Research Institute."

References

Alessio S M 2016 *Digital Signal Processing and Spectral Analysis for Scientists: Concepts and Applications* (Springer International Publishing) Online: https://www.springer.com/gp/book/9783319254661

Angeli S, Emblem K E, Due-Tonnessen P and Stylianopoulos T 2018 Towards patient-specific modeling of brain tumor growth and formation of secondary nodes guided by DTI-MRI *NeuroImage: Clinical* 20 664–73

Ayensa-Jiménez J, Pérez-Aliacar M, Randelovic T, Oliván S, Fernández L, Sanz-Herrera J A, Ochoa I, Doweidar M H and Doblaré M 2020 Mathematical formulation and parametric analysis of in vitro cell models in microfluidic devices: application to different stages of glioblastoma evolution *Scientific Reports* 10 21193

Binder B J and Simpson M J 2015 Spectral analysis of pair-correlation bandwidth: application to cell biology images *Royal Society Open Science* 2 140494

Bogdańska M U, Bodnar M, Piotrowska M J, Murek M, Schucht P, Beck J, Martínez-González A and Pérez-García V M 2017 A mathematical model describes the malignant transformation of low grade gliomas: Prognostic implications *PLOS ONE* 12 e0179999

Borasi G, Nahum A, Paulides M M, Powathil G, Russo G, Fariselli L, Lamia D, Cirincione R, Forte G I, Borrazzo C, Caccia B, di Castro E, Pozzi S and Gilardi M C 2016 Fast and high temperature hyperthermia coupled with radiotherapy as a possible new treatment for glioblastoma *J Ther Ultrasound* 4 Online: https://www.ncbi.nlm.nih.gov/pmc/articles/PMC5143464/

Bowers H J, Fannin E E, Thomas A and Weis J A 2020 Characterization of multicellular breast tumor spheroids using image data-driven biophysical mathematical modeling *Scientific Reports* 10 11583

Cooper L A D, Saltz J H, Catalyurek U and Huang K 2011 Acceleration of Two Point Correlation Function Calculation for Pathology Image Segmentation *2011 IEEE First International Conference on Healthcare Informatics, Imaging and Systems Biology* 2011 IEEE First International Conference on Healthcare Informatics, Imaging and Systems Biology pp 174–81

Cooper L, Saltz J, Machiraju R and Huang K 2010 Two-Point Correlation as a Feature for Histology Images: Feature Space Structure and Correlation Updating *Conf Comput Vis Pattern Recognit Workshops* 79–86

Gatenby R A and Gawlinski E T 1996 A reaction-diffusion model of cancer invasion *Cancer Res* 56 5745–53

Gerlee P and Nelander S 2012 The impact of phenotypic switching on glioblastoma growth and invasion *PLoS Comput Biol* 8 e1002556

Hathout L, Ellingson B and Pope W 2016 Modeling the efficacy of the extent of surgical resection in the setting of radiation therapy for glioblastoma *Cancer Sci* 107 1110–6

Hatzikirou H, Chauviere A, Bauer A L, Leier A, Lewis M T, Macklin P, Marquez-Lago T T, Bearer E L and Cristini V 2012 Integrative physical oncology *WIREs Systems Biology and Medicine* 4 1–14

Henares-Molina A, Benzekry S, Lara P C, García-Rojo M, Pérez-García V M and Martínez-González A 2017 Non-standard radiotherapy fractionations delay the time to malignant transformation of low-grade gliomas *PLoS One* 12 e0178552

Holdsworth C H, Corwin D, Stewart R D, Rockne R, Trister A D, Swanson K R and Phillips M 2012 Adaptive IMRT using a multiobjective evolutionary algorithm integrated with a diffusion–invasion model of glioblastoma *Phys. Med. Biol.* 57 8271–83

Irving J H and Kirkwood J G 1950 The Statistical Mechanical Theory of Transport Processes. IV. The Equations of Hydrodynamics *J. Chem. Phys.* 18 817–29

Jarrett A M, Hormuth D A, Barnes S L, Feng X, Huang W and Yankeelov T E 2018 Incorporating drug delivery into an imaging-driven, mechanics-coupled reaction diffusion model for predicting the response of breast cancer to neoadjuvant

chemotherapy: theory and preliminary clinical results *Phys Med Biol* 63 105015

Khetan J, Shahinuzzaman M, Barua S and Barua D 2019 Quantitative Analysis of the Correlation between Cell Size and Cellular Uptake of Particles *Biophys J* 116 347–59

Kibis and Buyuktahtakin 2018 Optimizing multi-modal cancer treatment under 3D spatio-temporal tumor growth - ScienceDirect Online: https://www.sciencedirect.com/science/article/abs/pii/S002555641730545X?via%3Dihub

Klank R L, Rosenfeld S S and Odde D J 2018 A Brownian dynamics tumor progression simulator with application to glioblastoma *Converg. Sci. Phys. Oncol.* 4 015001

Landau L D and Lifshits E M 1974 *Quantum Mechanics. Nonrelativistic theory*

Mang A, Bakas S, Subramanian S, Davatzikos C and Biros G 2020 Integrated Biophysical Modeling and Image Analysis: Application to Neuro-Oncology *Annu Rev Biomed Eng* 22 309–41

Martinez-Gonzalez A, Perez Romasanta L and Perez-Garcia V M 2012 Hypoxic Cell Waves Around Necrotic Cores in Glioblastoma: A Biomathematical Model and Its Therapeutic Implications | SpringerLink Online: https://link.springer.com/article/10.1007/s11538-012-9786-1

Mosaliganti K, Janoos F, Irfanoglu O, Ridgway R, Machiraju R, Huang K, Saltz J, Leone G and Ostrowski M 2009 Tensor classification of N-point correlation function features for histology tissue segmentation *Med Image Anal* 13 156–66

Narasimhan S, Johnson H B, Nickles T M, Miga M I, Rana N, Attia A and Weis J A 2019 Biophysical model-based parameters to classify tumor recurrence from radiation-induced necrosis for brain metastases *Med Phys* 46 2487–96

Nuttall A 1981 Some windows with very good sidelobe behavior *IEEE Transactions on Acoustics, Speech, and Signal Processing* 29 84–91

Pally D, Pramanik D and Bhat R 2019 An Interplay Between Reaction-Diffusion and Cell-Matrix Adhesion Regulates Multiscale Invasion in Early Breast Carcinomatosis *Front. Physiol.* 10 Online: https://www.frontiersin.org/articles/10.3389/fphys.2019.00790/full

Pasetto S, Crnojević D, Busso G, Chiosi C and Cassarà L P 2019 Theory of multiple-stellar population synthesis in a non-Hamiltonian setting *\na* 66 20–30

Pasetto S, Enderling H, Gatenby R A and Brady-Nicholls R 2021a Intermittent Hormone Therapy Models Analysis and Bayesian Model Comparison for Prostate Cancer *Bull Math Biol* 84 2

Pasetto S, Gatenby R A and Enderling H 2021b Bayesian Framework to Augment Tumor Board Decision Making *JCO Clinical Cancer Informatics* 508–17

Patel V and Hathout L 2017 Image-driven modeling of the proliferation and necrosis of glioblastoma multiforme *Theor Biol Med Model* 14 Online: https://www.ncbi.nlm.nih.gov/pmc/articles/PMC5414170/

Peebles P J E 1973 Statistical Analysis of Catalogs of Extragalactic Objects. I. Theory *The Astrophysical Journal* 185 413–40

Ridgway R, Irfanoglu O, Machiraju R, Huang K, Wenzel P, Debruin A and Leone G 2006 Image segmentation with tensor-based classification of n-point correlation functions *MICCAI Workshop on Medical Image Analysis with Applications in Biology* vol 1 (Citeseer)

Riley K F, Hobson M P and Bence S J 2006 Mathematical Methods for Physics and Engineering: A Comprehensive Guide *Higher Education from Cambridge University Press* Online: https://www.cambridge.org/highereducation/books/mathematical-methods-for-physics-and-engineering/FC466374D5B94E86D969100070CA6483

Roniotis A, Marias K, Sakkalis V, Manikis G C and Zervakis M 2012 Simulating radiotherapy effect in high-grade glioma by using diffusive modeling and brain atlases *J Biomed Biotechnol* 2012 715812

Roque T, Risser L, Kersemans V, Smart S, Allen D, Kinchesh P, Gilchrist S, Gomes A L, Schnabel J A and Chappell M A 2018 A DCE-MRI Driven 3-D Reaction-Diffusion Model of Solid Tumor Growth *IEEE Trans Med Imaging* 37 724–32

Sego T J, Glazier J A and Tovar A 2020 Unification of aggregate growth models by emergence from cellular and intracellular mechanisms *Royal Society Open Science* 7 192148

Swanson K R, Alvord E C and Murray J D 2000 A quantitative model for differential motility of gliomas in grey and white matter *Cell Prolif* 33 317–29

Swanson K R, Alvord E C and Murray J D 2002 Virtual brain tumours (gliomas) enhance the reality of medical imaging and highlight inadequacies of current therapy *Br J Cancer* 86 14–8

Swanson K R, Bridge C, Murray J D and Alvord E C 2003 Virtual and real brain tumors: using mathematical modeling

to quantify glioma growth and invasion *J Neurol Sci* 216 1–10

Swanson K R, True L D, Lin D W, Buhler K R, Vessella R and Murray J D 2001 A Quantitative Model for the Dynamics of Serum Prostate-Specific Antigen as a Marker for Cancerous Growth: An Explanation for a Medical Anomaly *The American Journal of Pathology* 158 2195–9

Szymanska Z, Urbanski, and Marciniak-Czochra 2009 Mathematical modelling of the influence of heat shock proteins on cancer invasion of tissue | SpringerLink Online: https://link.springer.com/article/10.1007/s00285-008-0220-0

Wang C H, Rockhill J K, Mrugala M, Peacock D L, Lai A, Jusenius K, Wardlaw J M, Cloughesy T, Spence A M, Rockne R, Alvord E C and Swanson K R 2009 Prognostic Significance of Growth Kinetics in Newly Diagnosed Glioblastomas Revealed by Combining Serial Imaging with a Novel Biomathematical Model *Cancer Res* 69 9133–40

Weis J A, Miga M I, Arlinghaus L R, Li X, Abramson V, Chakravarthy A B, Pendyala P and Yankeelov T E 2015 Predicting the Response of Breast Cancer to Neoadjuvant Therapy Using a Mechanically Coupled Reaction–Diffusion Model *Cancer Res* 75 4697–707

Weis J A, Miga M I, Arlinghaus L R, Li X, Chakravarthy A B, Abramson V, Farley J and Yankeelov T E 2013 A mechanically coupled reaction–diffusion model for predicting the response of breast tumors to neoadjuvant chemotherapy *Phys. Med. Biol.* 58 5851–66

Weis J A, Miga M I and Yankeelov T E 2017 Three-dimensional image-based mechanical modeling for predicting the response of breast cancer to neoadjuvant therapy *Computer Methods in Applied Mechanics and Engineering* 314 494–512

A

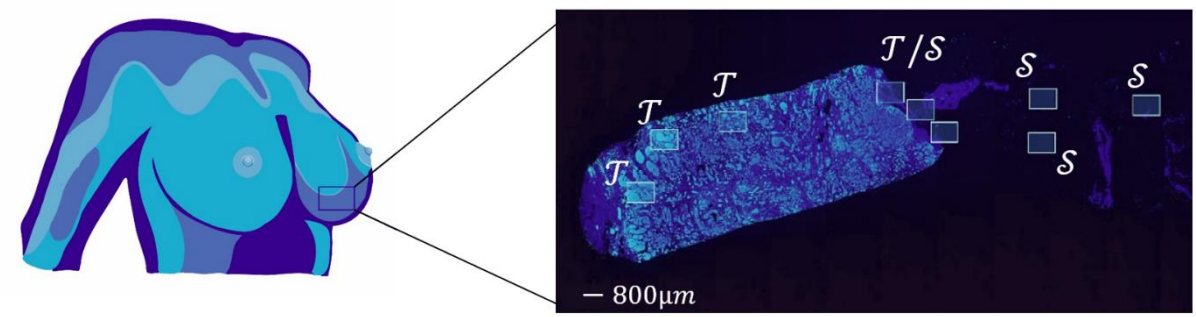

B

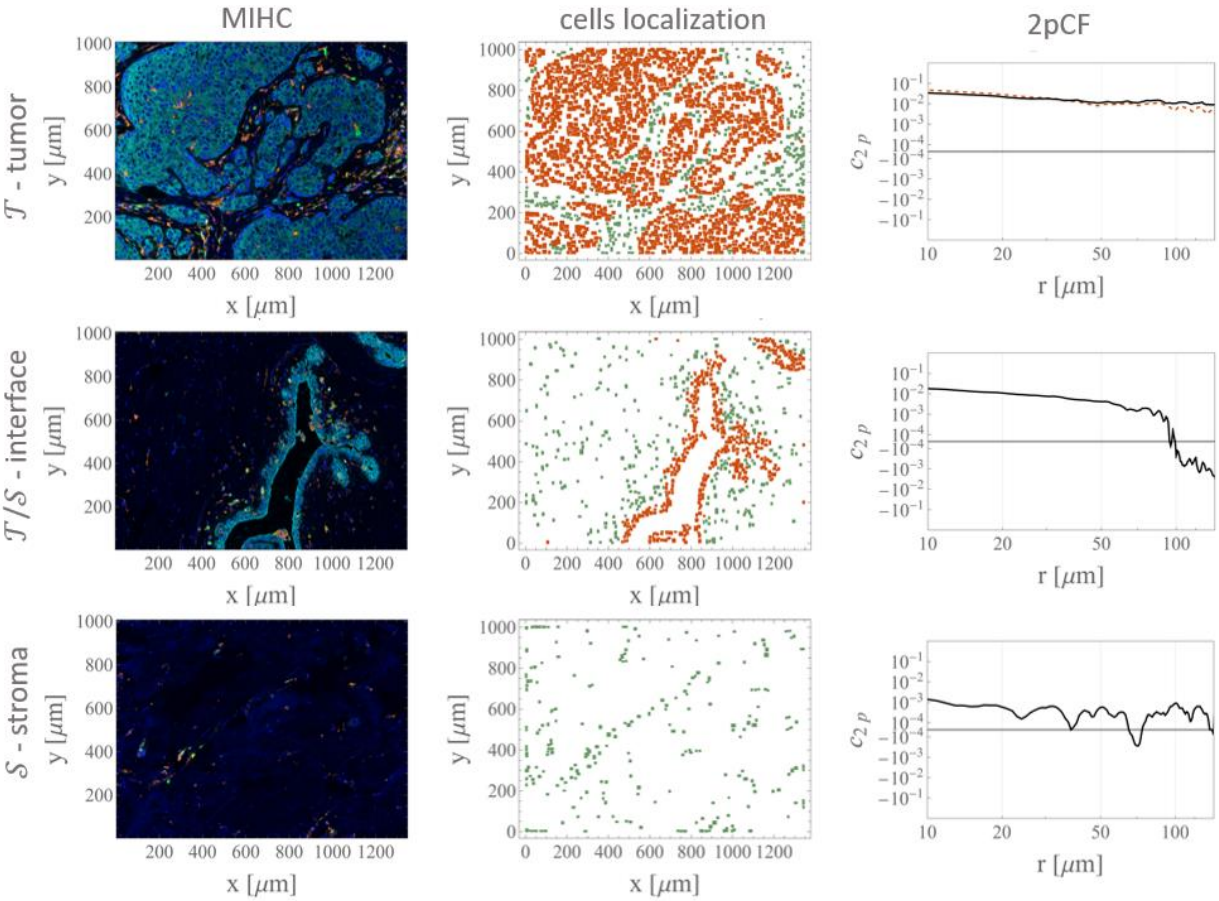

Figure 1. Patients' resection area analysis. Panel A: *a pictorial representation of tissue resection areas process.* ***Panel B****: stained images (left column), cell localization (central column), and 2pCF (right column) for the tumoral, interface, and stromal ROI (top, central and bottom rows, respectively). The brown dashed curve in the top panel of the right column shows the 2pCF for only cancer cells. We use red for the tumor and green for all the other components in the localization plot column. In the third column, we see the characteristic trends of the 2pCF for ROI with the presence of cancer (solid, positive correlation), for the interface areas (dropping curve with anticorrelation in the outer ROI), and for the stroma ROI (small positive correlation with random irregular areas of anticorrelation) bordering the noise frequency detection thresholds.*

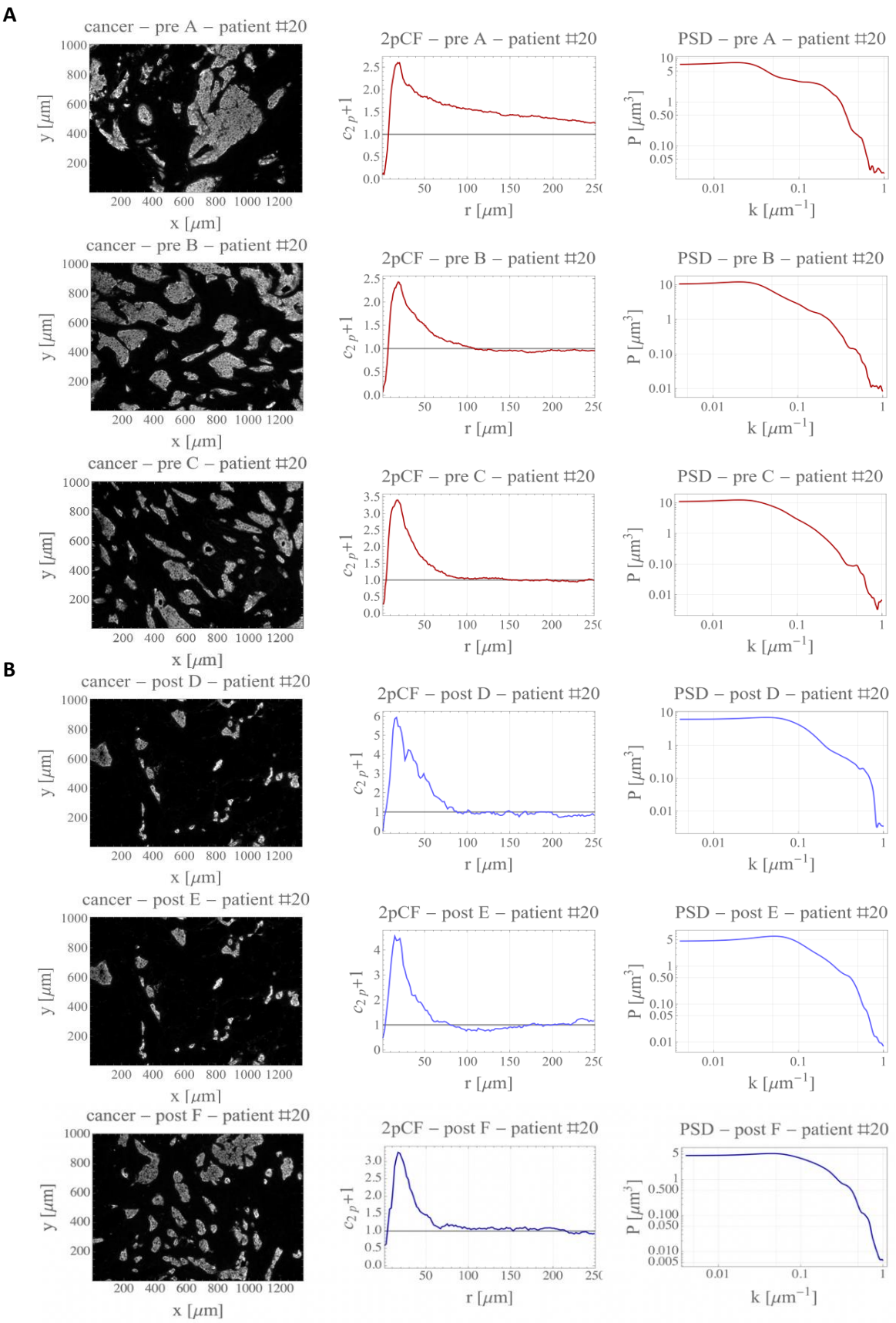

Figure 2. Power spectral analysis of cancer cell distribution. *Panel a: (left column) spatial distribution monochromatic-stained for some patient-#20 tumoral resection areas (sites A, B, and C, the first three rows) referring to pre-treatment biopsy. On the central column, the corresponding 2pCF, on the right column the PSD. Panel B: as Panel A but for post-treatment biopsy.*

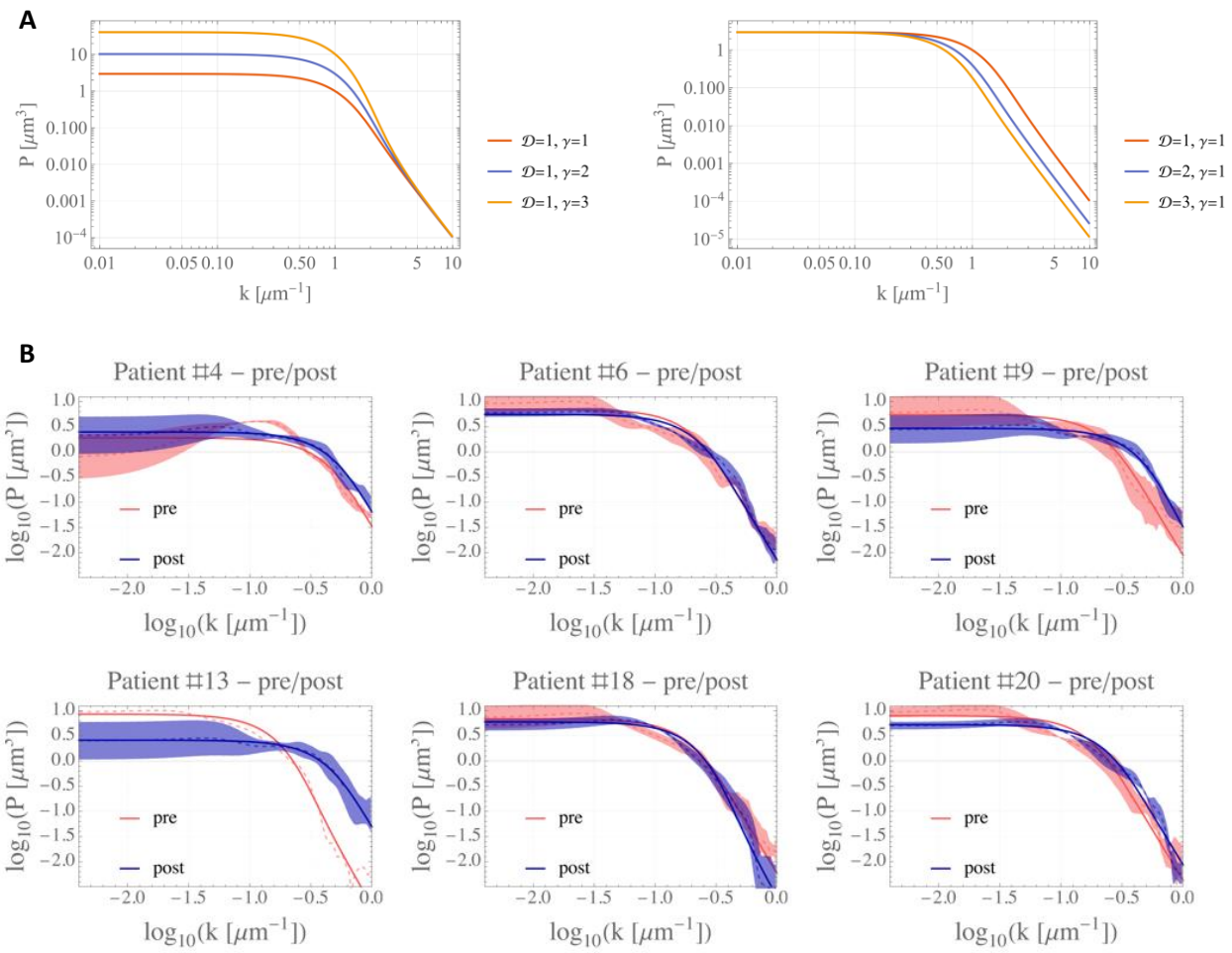

Figure 3. A. Power spectral density from RD framework. *PSD contribution is shown for an arbitrarily chosen set of parameters to evidence the different contributions of the reaction and diffusion coefficients at different wavenumbers.* ***B. Power spectral density pre-and post-treatment for several patients****. The solid curve refers to the RD model fit to the three pre-SBRT ROI (A, B, C; red) and the three post-SPRT ROI (D, E, F; blue). Dashed curves are the averages, and transparent shaded areas show standard error.*

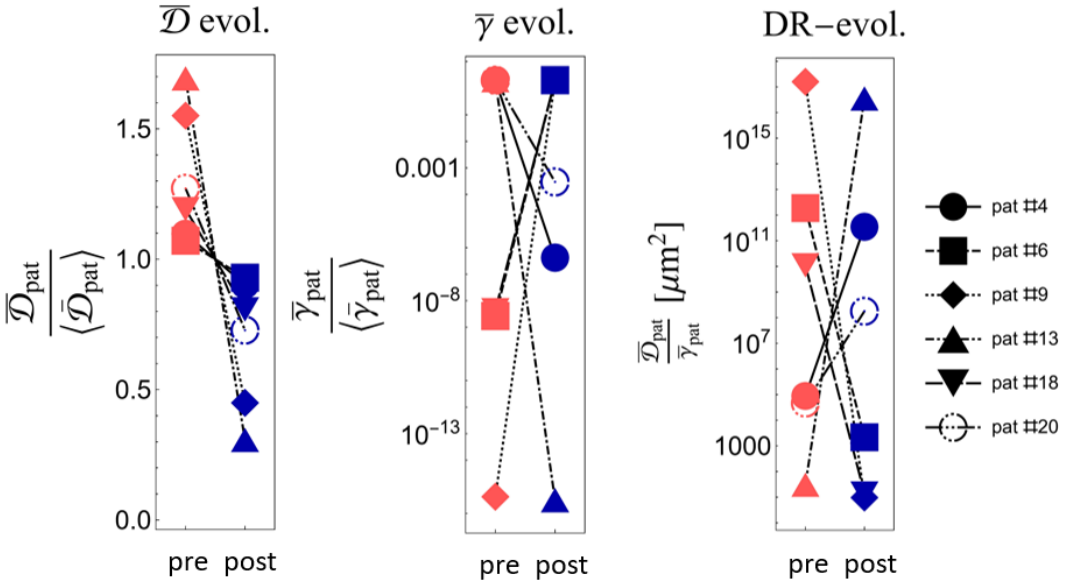

Figure 4. Comparison of pre-and-post-SABR reaction-diffusion parameters. ***A.*** *Spatially averaged across all $\mathcal{T}$ ROI per-patient diffusion parameters, $\overline{\mathcal{D}}_{pat}$, normalized by the time-averaged patient-specific diffusion parameter, $\langle\overline{\mathcal{D}}_{pat}\rangle$, across all $\mathcal{T}$ ROI for all times (pre and post).* ***B.*** *Same as A for the growth rates.* ***C.*** *Ration of the two coefficients.*